Spike mutation resilient scFv76 antibody counteracts SARS-CoV-2 lung damage upon aerosol delivery

Ferdinando M. Milazzo,[1,10] Antonio Chaves-Sanjuan,[2,3,10] Olga Minenkova,[1] Daniela Santapaola,[1] Anna M. Anastasi,[1] Gianfranco Battistuzzi,[1] Caterina Chiapparino,[1] Antonio Rosi,[1] Emilio Merlo Pich,[1] Claudio Albertoni,[4] Emanuele Marra,[5] Laura Luberto,[5] Cécile Viollet,[6] Luigi G. Spagnoli,[7] Anna Riccio,[8] Antonio Rossi,[9] M. Gabriella Santoro,[8,9] Federico Ballabio,[2] Cristina Paissoni,[2] Carlo Camilloni,[2] Martino Bolognesi,[2,3] and Rita De Santis[1]

[1]Biotechnology R&D, Alfasigma SpA, Via Pontina Km 30.400, Pomezia, 00071 Rome, Italy; [2]Department of Biosciences, University of Milan, Via Celoria 26, 20133 Milan, Italy; [3]Cryo-EM Lab, Pediatric Research Center, Fondazione Romeo e Enrica Invernizzi, University of Milan, Via Celoria 26, 20133 Milan, Italy; [4]Studio E Roma S.r.l., Via di Tor Vergata 434, 00133 Rome, Italy; [5]Takis Srl, Via di Castel Romano 100, 00128 Rome, Italy; [6]Texcell, Génavenir 5, Rue Pierre Fontaine 1, 91058 Evry Cedex, France; [7]Histo-Cyto Service Srl, Via Bernardino Ramazzini 93, 00151 Rome, Italy; [8]Department of Biology, University of Rome Tor Vergata, Via della Ricerca Scientifica 1, 00133 Rome, Italy; [9]Institute of Translational Pharmacology, CNR, Via Fosso del Cavaliere 100, 00133 Rome, Italy

The uneven worldwide vaccination coverage against severe acute respiratory syndrome coronavirus 2 (SARS-CoV-2) and emergence of variants escaping immunity call for broadly effective and easily deployable therapeutic agents. We have previously described the human single-chain scFv76 antibody, which recognizes SARS-CoV-2 Alpha, Beta, Gamma and Delta variants. We now show that scFv76 also neutralizes the infectivity and fusogenic activity of the Omicron BA.1 and BA.2 variants. Cryoelectron microscopy (cryo-EM) analysis reveals that scFv76 binds to a well-conserved SARS-CoV-2 spike epitope, providing the structural basis for its broad-spectrum activity. We demonstrate that nebulized scFv76 has therapeutic efficacy in a severe hACE2 transgenic mouse model of coronavirus disease 2019 (COVID-19) pneumonia, as shown by body weight and pulmonary viral load data. Counteraction of infection correlates with inhibition of lung inflammation, as observed by histopathology and expression of inflammatory cytokines and chemokines. Biomarkers of pulmonary endothelial damage were also significantly reduced in scFv76-treated mice. The results support use of nebulized scFv76 for COVID-19 induced by any SARS-CoV-2 variants that have emerged so far.

INTRODUCTION

Lung infection from emerging viruses can raise serious public health concern in the case of pandemics. From the coronavirus disease 2019 (COVID-19) pandemic, caused by the severe acute respiratory syndrome coronavirus 2 (SARS-CoV-2), we learned how a broad and timely vaccination campaign, together with adoption of prevention measures like mask wearing and social distancing and use of antiviral medications, can reduce deaths and intensive care pressure. The relatively milder disease recently associated with emergence of the Omicron BA.1 and BA.2 variants is raising hope for a weakening of the pandemic.[1] However, because of the uneven worldwide vaccination coverage and possible emergence of new viral variants escaping immunity, the evolution of COVID-19 is unpredictable, and re-occurrence of severe pulmonary diseases cannot be ruled out.[2] The observation of several threatening post-acute sequelae of SARS-CoV-2 infection particularly affecting the nervous and cardiovascular systems,[3] urgently necessitates easily deployable therapeutic measures able to control the infection in the early stages. With prospective COVID-19 pandemic re-exacerbation, and even in the case of transition into an endemic phase, two types of interventions are being envisaged: first, to improve vaccine equity worldwide with a possible update against SARS-CoV-2 variants and second, to validate early-stage therapeutic protocols preventing worsening of the disease and ultimately hospitalizations and post-acute sequelae. As of today, Omicron variants are challenging the efficacy of most injected antibodies.[4–10] Because the Omicron variants apparently remain confined mainly to the upper respiratory tract,[11] use of systemic antibodies is becoming somehow questionable.

We recently described a cluster of human anti-SARS-CoV-2 antibodies in the format of a single-chain variable fragment (scFv) able to neutralize viral variants *in vitro* and in animal models.[12] We also showed that such an antibody format is suitable for intra-nasal or aerosol formulations that might be useful for topical treatment of upper and lower respiratory tract SARS-CoV-2 infection.[12]

Correspondence: Rita De Santis, Biotechnology R&D, Alfasigma SpA, Via Pontina Km 30.400, Pomezia, 00071 Rome, Italy.
E-mail: rita.desantis@alfasigma.com

Table 1. ScFv76 spike/ACE2 competition by ELISA

	IC50 (nM) (±SE)		
	Delta	Omicron BA.1	Omicron BA.2
scFv76	1.64 (0.25)	1.90 (0.3)	2.4 (0.1)
scFv5	>40	>40	>40

Shown is competition of spike binding to human ACE2 by scFv antibodies, measured by ELISA. IC50 values (expressed as nanomolar concentration) are the average (±SE) from 3–4 independent experiments.

Table 2. ScFv76 surface plasmon resonance (SPR) data

Spike trimer	k_a (10^5 M^{-1} s^{-1})	k_d (10^{-5} s^{-1})	K_D (nM)
Delta	1.1	6.1	0.6
Omicron BA.1	0.7	41.6	6.3
Omicron BA.2	1.2	174.9	14.5

In the present work, we show that the scFv76 antibody of the cluster found previously to be able to react with SARS-CoV-2 Alpha, Beta, Gamma, and Delta is also resilient to the Omicron BA.1 and BA.2 mutations, substantially retaining neutralizing activity against these new viral variants. We provide a pre-clinical proof of concept of the efficacy of nebulized scFv76 in a mouse model of Delta infection, selected as an aggressive prototype of viral pneumonia. Finally, we prove, by single-particle cryoelectron microscopy (cryo-EM), the wide recognition properties of the scFv76 antibody at the molecular level, showing that it binds to a well-conserved epitope at the tip of the spike protein in the receptor binding domain (RBD) with an architecture that is able to accommodate the mutations found in all SARS-CoV-2 variants known to date. Our results support use of the scFv76 antibody for aerosol therapy of COVID-19 induced by all variants of concern.

RESULTS

ScFv76 efficiently neutralizes SARS-CoV-2 Delta and Omicron

The scFv76 antibody has been described previously to be able to neutralize the SARS-CoV-2 Alpha, Beta, Gamma, and Delta viral variants in vitro and in animal models.[12] To evaluate its reactivity with the recently emerged Omicron variants, the ability to compete the binding of the Omicron BA.1 and BA.2 spikes to human ACE2 was tested by ELISA. The results in Table 1 show that scFv76 can inhibit Omicron BA.1 and BA.2 spike binding to ACE2 at half maximal inhibitory concentration (IC50) concentrations of less than 2.5 nM, which is like the potency against Delta. The binding affinity of scFv76 to the Delta and Omicron spikes was then tested by Surface Plasmon Resonance (SPR) showing K_D values of 0.6 nM for Delta and 6.3 and 14.5 nM for BA.1 and BA.2, respectively (Table 2). Neutralizing activity against SARS-CoV-2 Omicron BA.1 and BA.2 pseudotyped viruses was also exhibited by scFv76 but not by scFv5 (an anti-RBD antibody shown previously to be devoid of neutralizing activity and used as a negative control),[12] with IC50 values of 2.84 and 2.47 nM, respectively (Figure 1A).

Neutralization of infectivity was further tested against authentic SARS-CoV-2 Delta and Omicron BA.1 viruses by microneutralization assay of cytopathic effects (CPEs) in Vero E6 cells. In this assay, scFv76 exhibited IC50 values of 1.99 and 6.38 nM against the Delta and Omicron BA.1 variants, respectively, whereas the non-neutralizing antibody scFv5 showed no anti-viral activity, as expected (Figure 1B).

The Omicron BA.2 spike has been shown recently to be more pathogenic and more efficient in mediating syncytium formation than the BA.1 spike.[13] The ability of scFv76 to prevent SARS-CoV-2 Omicron BA.1 or BA.2 spike-induced fusion of pulmonary cells was therefore tested in vitro. As shown in Figure 1C, incubation with nanomolar concentrations of the scFv76 antibody proved to be significantly effective at inhibiting fusion between BA.1 and BA.2 spike-expressing human HEK293T cells and human lung A549 cells stably expressing the hACE2 receptor (A549 hACE2).

Before an in vivo pharmacology study of nebulized scFv76 in a severe Delta-induced pneumonia mouse model, its antiviral neutralization potency was tested in vitro by qRT-PCR in Delta-infected pulmonary Calu-3 cells in comparison with the non-neutralizing control antibody scFv5. As shown in Figure 1D, scFv76 was found to inhibit infection with an IC50 of 13.5 nM, whereas no activity of the control antibody at a concentration greater than 200 nM was observed.

Therapeutic efficacy of nebulized scFv76 in a severe SARS-CoV-2 Delta interstitial pneumonia model

We previously established the biochemical suitability of scFv76 to aerosol delivery by a mesh nebulizer.[12] To test the pharmacological efficacy of the nebulized antibody, pneumonia infection was established in transgenic hACE2 mice by intranasal challenge with 1×10^5 50% tissue culture infectious dose (TCID50) SARS-CoV-2 (strain Delta B.1.617.2). The overall experimental design is shown in Figure 2A. Different from infected mice treated with vehicle, the group of mice treated with scFv76 showed significant body weight recovery 4 days after infection (Figure 2B). This result correlated with an about 100-fold reduction in lung viral RNA copy numbers, as assessed by qRT-PCR (Figure 2C), and with a reduction of infectious viral particles, as measured by TCID50 (Figure 2D). Nebulized scFv76 reduced infectious virus titers in the lungs to undetectable levels in three of five mice; significant viral RNA reduction was also observed in the nasal turbinates (Figure 2E). Histopathological analysis of lung sections showed a significant reduction of lung interstitial edema and hematic endoalveolar extravasation, a reduction of cellular inflammatory infiltrates in the alveolar/interstitial space, and a reduction of alveolar septal thickening (Figure 3A). Overall, treatment with nebulized scFv76, but not phosphate-buffered-saline (PBS), was significantly effective at counteracting the lung inflammation and damage induced by the Delta virus, as shown in Figure 3B. To further evaluate the extent of protection conferred by scFv76 nebulization in Delta-infected mice, qRT-PCR analyses were performed to measure the mRNA expression of several inflammatory effectors in lung homogenates harvested 4 days after infection. Data indicate that aerosol
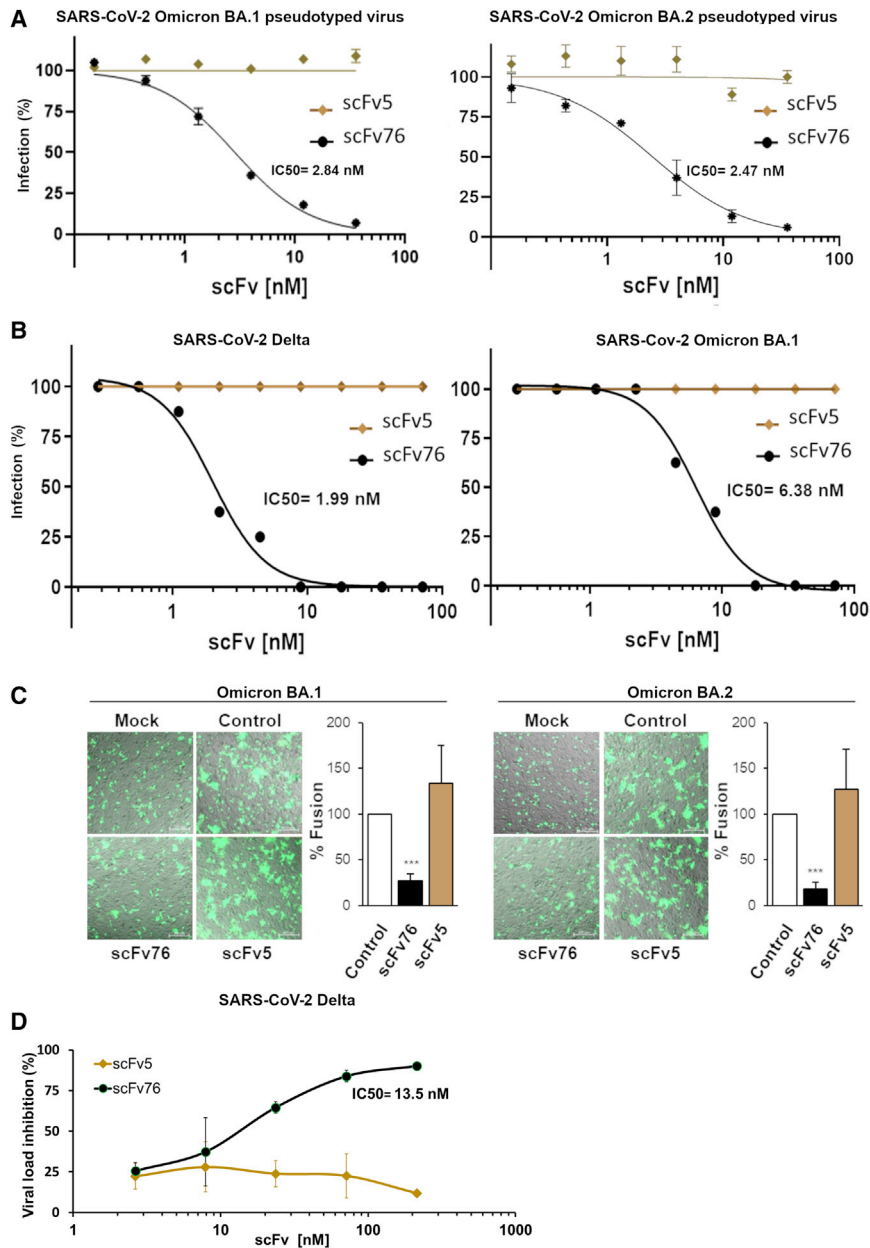
Figure 1. Resilience of scFv76 reactivity to the Omicron BA.1 and BA.2 variants

(A) Neutralization of pseudotyped virus expressing the SARS-CoV-2 Omicron (B.1.1.529) BA.1 or BA.2 spike, assessed by luciferase assay in hACE2-expressing Caco-2 cells. Data are the average (±SD) of two replicates from one representative experiment. (B) Neutralization activity of scFv antibodies assessed by viral titration (Delta and Omicron strains) on Vero E6 cells by microneutralization assay. Data are the average (±SD) of eight replicates from one representative experiment. (C) Inhibition of SARS-CoV-2 spike-mediated cell-cell fusion using HEK293T donor cells expressing green fluorescent protein (GFP) and Omicron BA.1 or BA.2 spike or GFP only (mock), incubated for 1 h with scFv76 or scFv5 (360 nM) and then overlaid on monolayers of hACE2-expressing A549 cells for 24 h. The overlay of bright-field and fluorescence images is shown. Scale bar, 200 μm. Cell-cell fusion quantification is expressed as percentage relative to control (average ± SD of 5 fields from two biological replicates). ***p < 0.001 (ANOVA). (D) Neutralization of the authentic SARS-CoV-2 Delta virus in Calu-3 cells. Serially diluted (3-fold) Abs were added to cells 1 h after infection. Quantification of viral load was done by qRT-PCR 72 h after infection. Data are the average (±SD) of two independent experiments. The IC50 value (expressed as nanomolar concentration) is also shown in (A), (B), and (D).

infection-induced tissue damage molecules, including adhesion molecules, angiopoietin 2, and inflammasome effectors such as NLRP3 (Figures 4D and 4E).

Structural bases for broad RBD recognition of SARS-CoV-2 variants by scFv76

To explore the recognition principles and rationalize the broad cross-reactivity of scFv76 toward SARS-CoV-2 variants, we determined the 3D structure of the spike:scFv76 complex using single-particle cryo-EM. We used a SARS-CoV-2 Wuhan-Hu-1 6P-stabilized glycoprotein (native antigen)[14] incubated with scFv76 to assemble the complex. Our single-particle cryo-EM analysis revealed a homogeneous population of the spike:scFv76 complex displaying two RBDs in the up conformation and one down, with one scFv76 fragment bound to the tip of each RBD (Figure 5A). The final 3D reconstruction had an overall resolution of 3.5 Å (Figures S1A and S2); nevertheless, the epitope-paratope interface regions were less clearly resolved compared with the main spike component because of flexibility of the RBDs. To gain better insight into the recognition interface structure, we applied a focused refinement procedure[15] to the RBD-down fragment region that brought the local resolution to 4.0 Å (Figures 5A, S1B, and S2) and subsequently based our analysis on this structure. The

treatment with scFv76 induced significant reduction of key pro-inflammatory cytokines like the interleukins IL6, IL1B, IL21, IL10, IL4, and tumor necrosis factor alpha (TNF) and the chemokines CCL2, CCL20, CXCL1, and CXCL10 (Figures 4A and 4B). The lungs of infected and vehicle-treated mice showed upregulated transcription levels of type I interferon (IFNA1 and especially IFNB1) and type II interferon (IFNG) and of key IFN-modulated genes (IFIT1, ISG15 and MX1). All of these genes were significantly reduced in lungs of mice treated with scFv76 (Figures 4A and 4C). Finally, we evaluated some biomarkers of pulmonary vascular damage, and the data indicated that the treatment also counteracted upregulation of
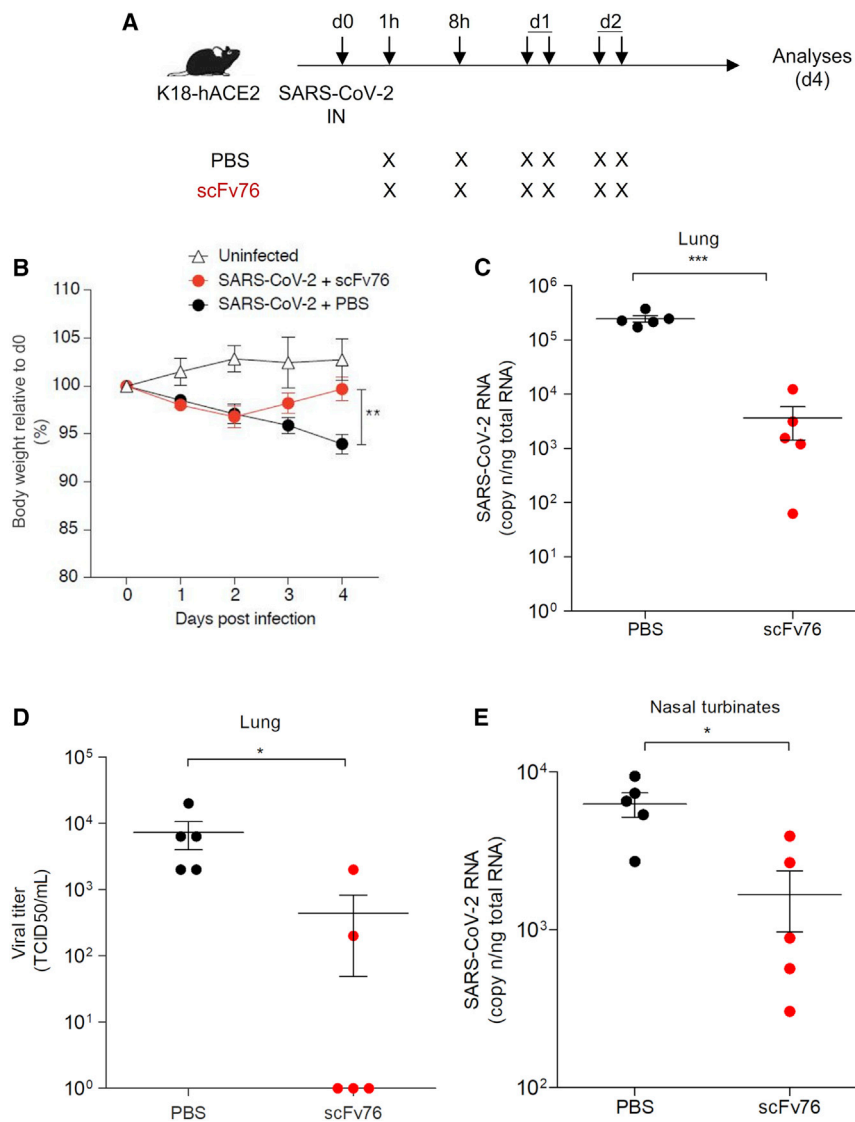
Figure 2. Therapeutic efficacy of nebulized scFv76 in a mouse SARS-CoV-2 Delta pneumonia model

(A) Study design. Human ACE2 transgenic mice were exposed by nose only to 2.5 mL of 3 mg/mL scFv76 solution or PBS (as vehicle control) 1 h and 8 h after SARS-CoV-2 Delta intranasal infection (1×10^5 TCID50/mouse) and twice per day for 2 additional days. (B) Body weight changes. Daily body weight from days 0–4 were recorded for each group and plotted as a percentage with respect to day 0. Data are the average (±SE). The day when there was a significant difference in average percentage of body weight between scFv76-treated or PBS-treated animals is denoted by $**p < 0.01$. (C) Lung viral RNA quantification. On day 4 after infection, lungs were collected for viral RNA quantification by qRT-PCR. Each dot represents one mouse. Data are expressed as copy number per nanogram of total RNA (n = 5). (D) Lung virus titration. Viral titers in the lung 4 days after infection were determined by viral 50% tissue culture infectious dose (TCID50) assay. Each dot represents one mouse. Data are expressed as TCID50 per milliliter. (E) Viral RNA quantification in nasal turbinates (NTs). Quantification by qRT-PCR in NTs and data representation were done as in (C). Statistical differences in (B–E) were assessed by Mann-Whitney U test. Significance is indicated as follows: $*p < 0.05$, $**p < 0.01$, $***p < 0.001$.

S56 (CDRH2), and the carbonyl groups of RBD residues L455 and A475 interact with Y33 and T28 (both in CDRH1), respectively; the side chain of RBD Y421 falls close to the P53 backbone carbonyl in CDRH2. The angle of approach of scFv76 to the RBD resembles that of ACE2; the scFv76 fragment contact region overlaps with the ACE2 binding interface, matching the location of 13 of 17 ACE2-binding residues on the RBD (Figure 5D). In this respect, the close resemblance of scFv76 and ACE2 binding modes to the RBD and the ensuing competition for binding explain, on structural grounds, the potent scFv76 neutralizing activity. The scFv76:RBD pose resembles closely that observed for most antibodies from the VH3-53/VH3-66 germline. Not all such antibodies show neutralizing activity across SARS-CoV-2 variants, again stressing the key role of subtle and specific structural variations in the outcome of epitope-paratope interaction.

A core of 28 epitope residues recognized by scFv76 is conserved in SARS-CoV-2 Alpha, Beta, Gamma, and Delta variants carrying the important K417N, E484K, and N501Y mutations (Table 3). In our refined model, E484 does not directly contact scFv76, consistent with the previously shown reactivity of scFv76 with E484-mutated variants.[12] We also predict low susceptibility to mutations at K417 and N501 because they are not involved in any polar contact with scFv76. Both residues are in solvent-exposed regions, allowing
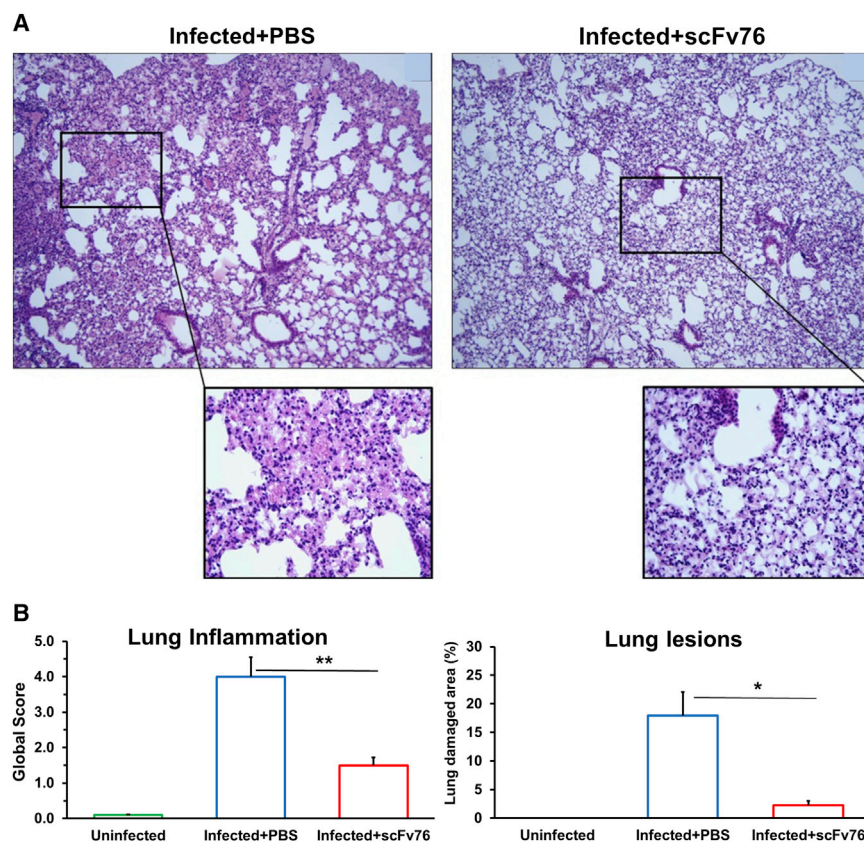
scFv76:RBD refined structure showed that the light and heavy chains of scFv76 contact the tip of the RBD in the up and down conformations. ScFv76 buries a surface area of ∼1,082 Å^2, based on an approximately equal contributions of the light and heavy chain components. The scFv76 paratope comprises residues of all three heavy-chain complementarity-determining regions (CDRs) and two from the light-chain CDRs (Table 3; Figure 5B). Conversely, the recognition site lies on the RBD receptor-binding ridge and surrounding areas (Figure 5C), in full agreement with an alanine scanning analysis reported previously,[12] where RBD L455A, F456A, Y473A, N487A and Y489A mutations strongly reduced scFv76 binding. F456 is located in the deep groove created between CDRH1 and CDRH2 on one side and CDRH3 and CDRL3 on the other. The scFv76:RBD interaction may also be stabilized by several hydrogen bonds (as evaluated on a 4.0-Å-resolution structure). Among these, RBD D420 interacts with

Figure 3. Therapeutic efficacy of nebulized scFv76 correlates with reduction of inflammatory scores

(A) Histopathological analysis of lung tissue sections from mice challenged with SARS-CoV-2 Delta and treated by aerosol with scFv76 or PBS, as described in Figure 2. Shown are representative pictures of lung sections, stained with hematoxylin and eosin (H&E), from PBS-treated (left panel) or scFv76-treated (right panel) mice. Scale bar, 200 μm; 10× magnification. Inset: 40× magnification. (B) Scores of overall lung inflammation (top panel) and lung lesion (bottom panel), measured on lung sections as in (A). Data are the average (±SE) (n = 5) and are expressed as global score and lung damaged area (percent), respectively (see scoring details in Materials and Methods). Statistical analysis was by Student's t test. Significance is indicated as follows: *p < 0.05, **p < 0.01.

DISCUSSION

In the search of easily deployable therapeutic measures against COVID-19, we recently described 76clAbs, a cluster of human single-chain antibody fragments that, in principle, could bypass all limitations of traditional monoclonal antibodies. Use of monoclonal antibodies for COVID-19 therapy is being challenged by several issues: (1) difficulties with deployment of therapy, being monoclonal antibodies parenteral drugs to be administered in a hospital environment; (2) the risk of antibody-dependent enhancement (ADE) that can be ignited by different routes involving the immunoglobulin Fc interaction with the Fc receptor[16] or with ACE2, found recently to possibly act as a secondary receptor,[17] or with Fcγ-expressing cells, including monocytes and macrophages that, by triggering inflammatory cell death, need to abort production of infectious virus and cause systemic inflammation that contributes to the severity of COVID-19 pathogenesis;[18] and (3) evasion properties of SARS-CoV-2 variants, particularly recently emerged Omicron lineages for which most approved and investigational antibodies have lost their neutralization activity.[4–10]

The single-chain antibody format, because of its high stability, can be easily used for self-administrable aerosol treatment. Single-chain antibodies are, in principle, devoid of ADE risk because of lack of an Fc sequence. 76clAbs, which were selected on the original SARS-CoV-2 Wuhan strain, were found to be resilient to Alpha, Beta, Gamma, and Delta variant mutations.[12] We show that the scFv76 antibody of the cluster can also recognize and neutralize the infectivity and fusogenic activity of Omicron BA.1 and BA.2 variants. Single-particle cryo-EM results point to the peculiar property of this antibody to bind to the up and down conformations of the spike RBD, recognizing a well-conserved epitope located at the ACE2 binding interface, thus accounting for its neutralization properties. All mutations in the RBD of the known SARS-CoV-2 variants are predicted to marginally affect scFv76 recognition, as confirmed by experimental results. We
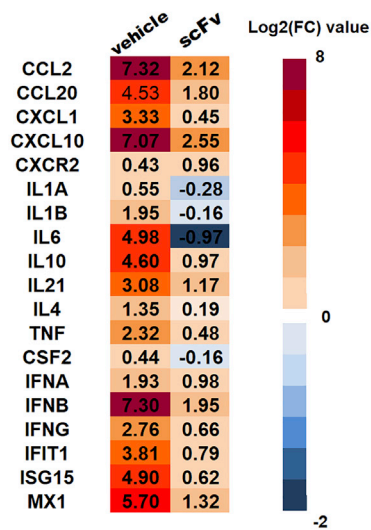
conformational flexibility; 417N would insert into a large groove created among CDRs, and 501Y would position the aromatic side chain beyond scFv76 CDRL3 (Figures 5C and S3). Both mutations are indeed known to have a limited effect on scFv76 neutralizing power,[12] in keeping with the broad SARS-CoV-2 recognition properties displayed by scFv76.

Our modeling exercise suggests that the residues building the RBD epitope, recognized by scFv76, should drop to 23 in the Omicron BA.1 and BA.2 spike variants (Table 3). This could explain the 10- and 20-fold affinity reduction for Omicron BA.1 and BA.2, respectively, compared with the Delta variant. In our model, the five Omicron-unique side-chain substitutions, occurring in the RBD epitope region in these variants, are predicted to marginally affect scFv76 binding, as confirmed by the RBD/ACE2 competition and virus neutralization data presented here. The S477N, Q493R, G496S, and Q498R substitutions in particular would place the mutated residues in solvent-exposed regions (Figures 5C and S3). Residue Y505 is located between CDRL1 and CDRL3 in the RBD:scFv76 complex and mostly participates in hydrophobic contacts (Figures 5C and S3); the Omicron Y505H mutation may follow the same scheme. Such considerations, supporting substantial conservation of the RBD:scFv76 interface in all variants, are in agreement with the functional data reported in this paper that highlight the resilience of scFv76 to the main SARS-CoV-2 variants, including Omicron BA.1 and BA.2.
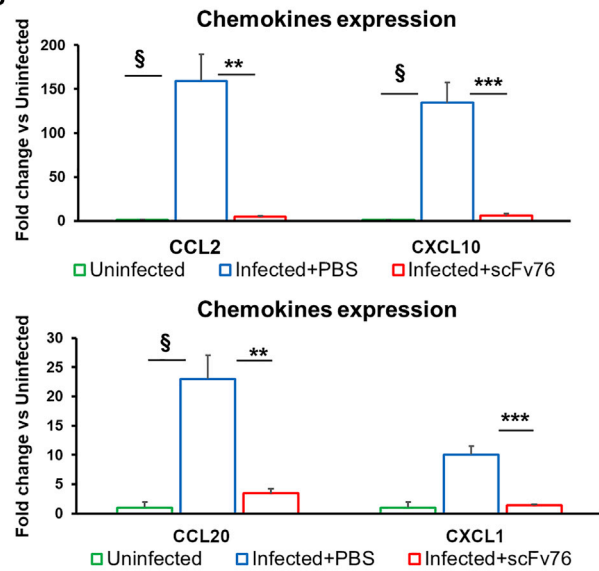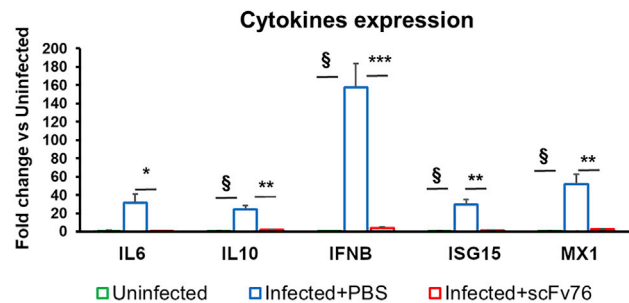
A

	vehicle	scFv
CCL2	7.32	2.12
CCL20	4.53	1.80
CXCL1	3.33	0.45
CXCL10	7.07	2.55
CXCR2	0.43	0.96
IL1A	0.55	-0.28
IL1B	1.95	-0.16
IL6	4.98	-0.97
IL10	4.60	0.97
IL21	3.08	1.17
IL4	1.35	0.19
TNF	2.32	0.48
CSF2	0.44	-0.16
IFNA	1.93	0.98
IFNB	7.30	1.95
IFNG	2.76	0.66
IFIT1	3.81	0.79
ISG15	4.90	0.62
MX1	5.70	1.32

Log2(FC) value

D

ANGPT2	2.68	1.75
CDH5	-1.92	-0.92
COX2	0.53	0.05
ICAM1	0.56	-0.98
NLRP3	1.49	0.14
SELE	4.62	1.95
VCAM1	1.03	-0.07

Log2(FC) value
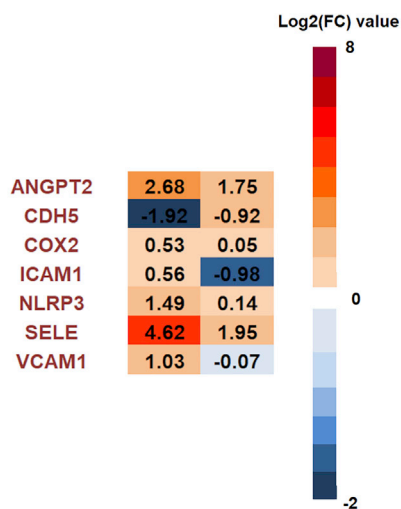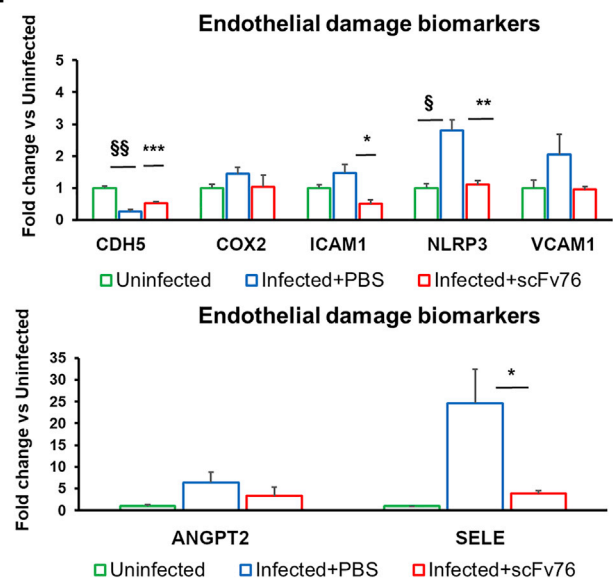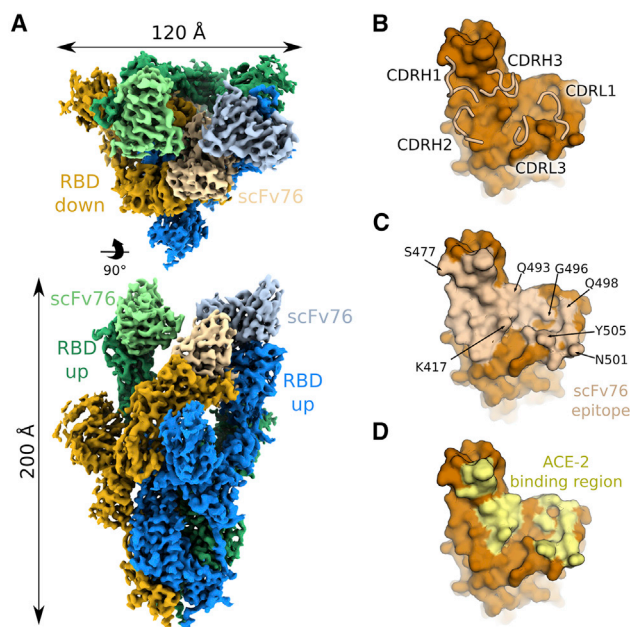
Figure 5. ScFv76 broad recognition of SARS-CoV-2 variants

(A) Composite cryo-EM map of the SARS-CoV-2 spike protein with the locally refined RBD:scFv76 in two orientations. The RBD up or down conformations with their corresponding scFv76 fragments are labeled. The spike subunits are highlighted in green, blue, and yellow, respectively, and the scFv76 fragments bound to each RBD are shown in light green, light blue, and light yellow. (B) ScFv76 CDR loops overlaid on the surface representation of the RBD. (C) RBD surface showing epitope residues as colored in (B). (D) RBD surface showing the ACE2 binding region in yellow.

hypothesize that the Omicron variants BA.4 and BA.5 might be still neutralized by scFv76. The spike mutated residues in these two variants, relative to Omicron BA.2, are 69-70del, L452R, F486V, and wild-type amino acid Q493,[19] with F486V the only mutation at the scFv76 binding interface. F486V replaces a bulky apolar side chain, closing a hydrophobic patch, with a smaller one, possibly affecting, to a limited degree, the stability of the complex.

Significant therapeutic efficacy of nebulized scFv76 is shown here in a severe model of SARS-CoV-2 Delta pneumonia. The present data indicate that aerosol treatment with scFv76 can efficiently control virus proliferation, significantly reducing lung inflammation and damage. These results encourage further clinical development of scFv76

Table 3.

Residues from the scFv76 heavy chain component contacting the RBD	
G26, F27, T28, A31, N32, Y33	from CDRH1
Y52, P53, G54, S56, F58	from CDRH2
R97, L99, S100, V101, A102, D106, I107	from CDRH3
Residues from scFv76 light chain component contacting the RBD	
Q160, S161, V162, S163, S164, Y166	from CDRL1
G226, S227, Y230	from CDRL3

Shown are SARS-CoV-2 RBD residues that are in contact with scFv76. Residues mutated in Alpha, Beta, Gamma, and Delta variants are shown in italics; residues mutated in Omicron BA.1 and BA.2 are displayed in italics and bold black, respectively: R403, T415, G416, *K417*, D420, Y421, T453, L455, F456, R457, K458, S459, N460, Y473, Q474, A475, G476, **S477**, F486, N487, Y489, **Q493**, S494, Y495, **G496**, **Q498**, T500, *N501*, V503, **Y505**.

antibody aerosol therapy as a new opportunity for treatment of COVID-19, regardless of the variant causing the disease.

MATERIALS AND METHODS

Spike/ACE2 binding competition

For competition experiments, Nunc MaxiSorp plates with 96 wells were coated with 100 μL/well of SARS-CoV-2 spike1 variant B.1.617.2 (Delta) protein (His tag) and SARS-CoV-2 spike S1+S2 trimer variant B.1.1.529 (Omicron) protein (ECD, His tag), both from Sino Biological, and SARS-CoV-2 spike trimer variant BA.2 (Omicron) protein His tag verified by Multiangle Light Scattering (MALS), from Acro Biosystems, in PBS at a final concentration of 0.5 μg/mL overnight (ON) at +4°C. Plates were blocked with 300 μL/well blocking solution for 2 h at room temperature (RT). After washing, dilutions of antibodies were added in a volume of 50 μL/well at double concentration, and after 30-min incubation at 37°C, 1.0 μg/mL human ACE2 protein mouse Fc tag (Sino Biological) was added and incubated for 1 h at 37°C. Plates were washed 4 times with PBS/Tween and then incubated for 1 h at RT with 100 μL/well of an anti-mouse Fc conjugated to alkaline phosphatase (Sigma-Aldrich), diluted 1:1,000 in blocking buffer. After washing 4 times, 100 μL/well p-nitrophenyl phosphate (pNpp) substrate was added, and plates were incubated at RT in the dark. Absorbance was recorded at 405 nm using a Sunrise Tecan spectrophotometer.

SPR

Kinetic constants were determined using SPR experiments with a Biacore T200 instrument (Cytiva). SARS-CoV-2 Spike trimer (T19R,

Figure 4. The therapeutic efficacy of nebulized scFv76 correlates with the reduction of pulmonary inflammatory and vascular damage biomarkers

(A) Heatmap of differential gene expression for inflammatory effectors, as determined by qRT-PCR, in lung homogenates of mice challenged with SARS-CoV-2 Delta and treated by aerosol with scFv76 or PBS. Data are the average of the log2 expression fold change (FC) obtained from each experimental group (n = 5) with respect to uninfected mice. Up-regulation appears as shades of red, and down-regulation appears as shades of blue. (B) The mRNA expression level of genes encoding for key chemokines, assessed by qRT-PCR in samples as in (A). Results are the average (±SE) of expression FC with respect to uninfected mice. (C) The mRNA expression levels of genes encoding for key inflammatory effectors, assessed by qRT-PCR as above. Results are expressed as in (C). (D) Heatmap of differential gene expression analysis for pulmonary vascular damage biomarkers. (E) The mRNA expression levels of key pulmonary vascular damage-related genes, assessed and represented as above. Statistical differences in (B), (C), and (E) were assessed by Student's t test. Significance is indicated as follows: §$p < 0.05$ and §§$p < 0.01$ infected + PBS-treated versus uninfected mice; *$p < 0.05$, **$p < 0.01$, and ***$p < 0.001$ infected + PBS-treated versus infected + scFv76-treated mice.

G142D, EF156-157del, R158G, L452R, T478K, D614G, P681R, and D950N) His tag (MALS verified) protein (Acro Biosystems), SARS-CoV-2 spike S1+S2 trimer variant B.1.1.529 (Omicron) protein (ECD, His tag, Sino Biological), and SARS-CoV-2 spike trimer variant BA.2 (Omicron) protein His tag (MALS verified, Acro Biosystems), all 1.25 μg/mL in buffer containing 0.01M Hepes pH 7.4, 0.15M NaCl, 0.005% w/w surfactant P20 (HBS-P+ from Cytiva), were immobilized at 1,000 Resonance Units (RU) level on the surface of a flow cell of a Series S sensor chip nitrilotriacetic acid (NTA from Cytiva) using Ni^{2+}-mediated capture followed by an amine coupling procedure, and another flow cell surface was blank immobilized by amine coupling with ethanolamine to be used as a control surface. Then scFv76 was flowed at 30 μL/min on all flow cells at 0.47, 1.40, 4.19, 12.56, 37.67, and 113 nM concentrations in buffer containing 10mM Hepes, 0.15M NaCl, 3mM EDTA disodium dihydrate, 0.005% w/w surfactant P20, pH 7.4 (HBS-EP+ buffer from Cytiva) for a contact time of 480 s. After a dissociation time of 900 s, all flow cell surfaces were regenerated by flowing a solution of 4 mM glycine-HCl and 0.1% sodium dodecyl sulphate (SDS) w/w at 30 μL/min for 30 s. Double-referenced sensorgrams were obtained by subtraction of blank-immobilized flow cell curves and of zero concentration curves from derivatized surface flow cell curves. Kinetic constants were obtained by BIAevaluation 3.2 software (Cytiva) fitting with a 1:1 binding model.

Virus neutralization in Calu-3 cells

To measure the SARS-CoV-2-neutralizing capability of scFv76, a live SARS-CoV-2 assay was performed by measuring the viral load in human lung adenocarcinoma Calu-3 cells by qRT-PCR 72 h after virus infection. The experiments were carried out at the François Hyafil Research Institute (Oncodesign; Villebon-sur-Yvette, France). Calu-3 cells were seeded in 96-well plates in complete cell culture medium consisting of Minimal Essential Medium (MEM), 1% pyruvate, 1% glutamine, and 10% fetal bovine serum and then infected, at a multiplicity of infection of 0.01, with SARS-CoV-2 Delta virus provided by the National Institute of Infectious Diseases (NIID) Japan, strain hCoV-19/Japan/TY11-330-P1/2021; originally provided by the Global Initiative on Sharing Avian Influenza Data (GISAID): EPI_ISL_ 2158613. One hour after infection, the virus solution was discarded and replaced by a volume of growth medium containing scFv76 or non-neutralizing scFv5 antibody at a concentration ranging from 214–2.6 nM in triplicate. The plates were then transferred to a 37°C incubator for 72 h. Finally, the cell culture supernatants were collected for viral RNA extraction (Macherey Nagel Viral RNA Kit), and viral RNA copy number was quantified by qRT-PCR, targeting a region in the viral ORF1ab gene and using a QuantStudio 7 Real-Time PCR System (Applied Biosystems). Data were processed using GraphPad Prism software (v.8.0), and the IC50 values were calculated using a four-parameter logistic curve fitting approach.

SARS-CoV-2 S-pseudovirus neutralization assays

Generation of SARS-CoV-2 S-pseudovirus and SARS-CoV-2 S-pseudovirus neutralization assays were performed as described previously.[12] The vectors expressing Omicron SARS-CoV-2-spike (S1+S2)-long (B.1.1.529) and SARS-CoV-2-spike (S1+S2)-long (B.1.1.529 sublineage BA.2) were obtained from GenScript and Sino Biological, respectively. Serial (1:3) dilutions (ranging from 35.7–0.14 nM final concentration) of scFvs were tested in duplicate. Luciferase activity (relative luciferase units [RLU]) was detected 72 h after infection using the Bright-Glo Luciferase Assay System Kit (Promega) in a microplate luminometer (Wallac-PerkinElmer).

Microneutralization assay

Neutralizing antibody titers were tested using a live-virus assay as follows. ScFv samples were pre-diluted in inoculation medium consisting of Dulbecco's Modified Eagle's Medium (DMEM), 2% fetal calf serum, 1% glutamine), followed by 9 serial dilutions in inoculation medium. Each serial dilution was then mixed 1:1 with 2,000 TCID50/mL SARS-CoV-2 variant virus (Delta variant strain hCoV-19/USA/MD-HP05647/2021 and Omicron variant strain hCoV-19/USA/MD-HP20874/2021) and incubated for 1 h at +37°C ± 2°C and 5% ± 0.5% of CO_2. Thirty-five microliters of each diluted sample/virus mix were then applied in octuplicate to Vero E6 cells seeded at a density of 10^4 cells/well in a 96-well plate on day −1. After 1 h of incubation at +37°C ± 2°C and 5% ± 0.5% CO_2, 65 μL of inoculation medium (DMEM, 2% fetal calf serum, 1% glutamine) was added per well. Plates were incubated for 6 days at +37°C ± 2°C, 5% ± 0.5% CO_2. After this incubation, the cells were inspected for CPEs, and the number of positive wells (that is, exhibiting CPEs) was recorded. Data were processed using GraphPad Prism software (v.8.0), and the IC50 values were calculated using a four-parameter logistic curve fitting approach.

Cell-cell fusion assay

Human alveolar type II-like epithelial A549 cells and HEK293T cells were obtained from the ATCC (Manassas, VA). Cells were grown at 37°C and 5% CO_2 in RPMI-1640 (A549 cells) or DMEM (HEK293T cells) (Euroclone) supplemented with 10% fetal calf serum (FCS), 2 mM glutamine, and antibiotics. Generation of A549 cells stably expressing the human ACE2 receptor (A549-hACE2 cells) has been described previously.[20] The vectors expressing Omicron SARS-CoV-2-spike (S1+S2)-long (B.1.1.529) and SARS-CoV-2-spike (S1+S2)-long (B.1.1.529 sublineage BA.2) were obtained from GenScript and Sino Biological, respectively. Transfections were performed using Lipofectamine 2000 (Invitrogen, Thermo Fisher Scientific) according to the manufacturer's instructions. The donor-target cell fusion assay has been described previously.[12] Transmission and fluorescence images were taken using a Carl Zeiss Axio Observer inverted microscope, and the extent of fusion was quantified as described previously.[12] Images shown in all figures are representative of at least five random fields (scale bars are indicated). Statistical analysis was performed using one-way ANOVA (GraphPad Prism 6.0 software, GraphPad). All experiments were done in duplicate and repeated at least twice.

In vivo pharmacological evaluation of nebulized scFv76 in a model of SARS-CoV-2 Delta pulmonary infection

The animal study was carried out at the San Raffaele Scientific Institute (Milan, Italy) and performed in accordance with European

Directive 2010/63/EU for protection of animals used for scientific purposes, applied in Italy by Legislative Decree 4 March 2014, n. 26. All experimental animal procedures were approved by the Institutional Animal Committee of San Raffaele Scientific Institute. Female transgenic K18-hACE2 mice, aged 8–10 weeks, were infected via the intranasal route with 1×10^5 TCID50/mouse of SARS-Cov-2 variant Delta B.1.617.2 virus (hCoV-19/Italy/LOM-Milan-UNIMI9615/2021 [GISAID: EPI_ISL_3073880]), obtained from the Laboratory of Microbiology and Virology of San Raffaele Scientific Institute. One hour and 8 h after infection and twice per day for 2 additional days, infected mice (5/group) were treated by nose-only nebulization with 2.5 mL of scFv76 (3.0 mg/mL in PBS) or PBS using an Aerogen Pro (Aerogen) mesh nebulizer and a nose-only inhalation chamber suitable for delivering the nebulized antibodies contemporarily for up to 8 mice, as described previously.[12] Mice were monitored for appearance, behavior, and weight. On day 4 after infection, they were euthanized by inhalation of 5% isoflurane, followed by gentle cervical dislocation, and lungs and nasal turbinates were explanted and then fixed by 4% paraformaldehyde for histopathological analyses or snap-frozen (in liquid nitrogen) and stored at -80°C until further analyses.

Tissue homogenization and viral titer determination

For viral titer determination in the lungs, tissue homogenates were prepared by homogenizing perfused lungs using a gentleMACS Octo dissociator (Miltenyi) in M tubes containing 1 mL of DMEM. Samples were homogenized three times with program m_Lung_01_02 (34 s, 164 rpm). The homogenates were centrifuged at 3,500 rpm for 5 min at 4°C. The supernatant was collected and stored at −80°C until use for viral isolation and viral load detection. Viral titer was calculated by TCID50. Briefly, Vero E6 cells were seeded at a density of 1.5×10^4 cells per well in flat-bottom 96-well tissue culture plates. The following day, 2-fold dilutions of the homogenized tissue were applied to confluent cells and incubated for 1 h at 37°C. Then cells were washed with phosphate-buffered saline (PBS) and incubated for 72 h at 37°C in DMEM and 2% FBS. Cells were fixed with 4% paraformaldehyde for 20 min and stained with 0.05% (w/v) crystal violet in 20% methanol. The plate analysis was carried out by qualitative visual assessment of CPEs. TCID50 was determined using the Reed and Muench method.

qRT-PCR for viral copy quantification and gene expression analysis

For viral copy quantification and gene expression analysis, tissue homogenates were prepared by homogenizing perfused lungs or nasal turbinates (NTs) using a gentleMACS dissociator (Miltenyi) with program RNA_02 in M tubes in 1 mL or 500 μL Trizol (Invitrogen) for lungs or NTs, respectively. The homogenates were centrifuged at $2,000 \times g$ for 1 min at 4°C, and then the supernatant was collected. RNA extraction was performed by combining phenol/guanidine-based lysis with silica membrane-based purification. Briefly, 100 μL of chloroform was added to 500 μL of homogenized sample; after centrifugation, the aqueous phase was added to 1 vol-

ume of 70% ethanol and loaded on a ReliaPrep RNA Tissue Miniprep column (Promega, catalog number Z6111). Total RNA was isolated according to the manufacturer's instructions. For viral copy quantification, quantitative polymerase chain reaction (qPCR) was performed using TaqMan Fast Virus 1 Step PCR Master Mix (Applied Biosystems); a standard curve was drawn with 2019_nCOV_N Positive control (Integrated DNA Technologies), and the following primers and probe were used: 2019-nCoV_N1 forward primer (5′-GAC CCC AAA ATC AGC GAA AT-3′), 2019-nCoV_N1 reverse primer (5′-TCT GGT TAC TGC CAG TTG AAT CTG-3′), and 2019-nCoV_N1 probe (5′-FAM-ACC CCG CAT TAC GTT TGG TGG ACC-BHQ1-3′) (Centers for Disease Control and Prevention [CDC] Atlanta, GA). All experiments were performed in duplicate.

For gene expression analysis of inflammation and endothelium-related genes, total RNA was retrotranscribed using SuperScript IV VILO Mastermix (Invitrogen, Thermo Fisher Scientific) according to the manufacturer's instructions. Quantitative real-time PCR was performed using TaqMan Fast Advanced Master Mix and specific TaqMan gene expression assays (listed in Table S1), both from Applied Biosystems (Thermo Fisher Scientific). The 7900HT Sequence Detection System instrument and software (Applied Biosystems) were used to quantify the mRNA levels of the target genes according to a six-point serial standard curve generated for each gene. The results were ultimately expressed, after normalization to the housekeeping gene Rlp32, as relative expression (fold change) compared with uninfected animals.

Histopathological analysis

PBS-perfused lungs were fixed in Zn-formalin for 24 h and then stored in 70% ethanol until trimming for paraffin wax embedding and the following histological examination. Consecutive sections (20 μm) were prepared and stained by the classic hematoxylin and eosin (H&E) method, and then microscopic observation was performed using a Nikon Eclipse 80i microscope equipped with a DXM1200F microscope camera. Pathological features in lung sections were scored as follows: inflammation-related parameters, including congestion of the alveolar septa, lymphomonocyte interstitial (alveolus) infiltrate, alveolar hemorrhage, interstitial edema, and platelet microthrombi, were evaluated separately by two independent pathologists, and the extent of these findings was scored arbitrarily using a two-tiered system: 0 (negative), 1 (moderate), and 2 (severe). All scores for each animal were ultimately summed up, and a global score was calculated for each group and expressed as the average ± SE. The percentage of pulmonary area affected by lesions in each section was also measured, and results for each group were reported as average percentage ± SE.

Electron microscopy sample preparation

A sample of SARS-CoV-2 Wuhan-Hu-1 6P-stabilized glycoprotein (native antigen) was incubated with scFv76 at a final concentration of 0.65 mg/mL and 0.22 mg/mL, respectively, for 1 h at RT. A 4-μL

droplet of the sample was applied onto an R1.2/1.3 300-mesh copper holey carbon grid (Quantifoil) previously glow discharged for 30 s at 30 mA using a GloQube system (Quorum Technologies). The sample was incubated on the grid for 60 s at 4°C and 100% relative humidity, blotted, and plunge-frozen in liquid ethane using a Vitrobot Mk IV (Thermo Fisher Scientific).

EM data collection and image processing
Cryo-EM data were acquired on a Talos Arctica (Thermo Fisher Scientific) transmission electron microscope operated at 200 kV. The data were acquired using EPU-2.8 automated data collection software (Thermo Fisher Scientific). Movies were collected at a nominal magnification of 120,000x, corresponding to a pixel size of 0.889 Å/pixel at the specimen level, with applied defocus values between −0.8 and −2.2 μm. A total of 4,211 movies were acquired using the Falcon 3 direct electron detector (Thermo Fisher Scientific) operating in electron counting mode, with a total accumulated dose of 40 e⁻/A2 distributed over 40 movie frames.

Movies were preprocessed with WARP 1.0.9.[21] A 5 × 5 × 40 model was used for motion correction using a 35-7 Å resolution range weighted with a −500 Å^2 B factor. Contrast transfer function (CTF) was estimated using the 40-3.5 Å resolution range and a 5 × 5 patch model. Particle picking was performed using the deep convolutional neural network BoxNet2Mask_20180918, resulting in 490,614 particles that were extracted in 400-pixel boxes and imported into CRYOSPARC-3.3.1[15] for further processing.

2D classification was used to select 366,967 particles that were 3D aligned using the SARS-CoV-2 spike glycoprotein model (EMDB: 21452) low pass filtered at 30 Å as a reference. Particles were subjected to 3D classification to select the final set of 87,623 particles that yielded an overall 3.5-Å resolution reconstruction based on the gold-standard criterion of 0.143 Fourier shell correlation (FSC) value. The initial reconstruction displayed two spike RBDs in the up conformation and one down, with all three showing one bound scFv76 fragment. Particles were subtracted with a mask comprising the entire spike molecule without the RBD in the down conformation and its corresponding scFv76 fragment and then locally refined to 4.0-Å resolution according to an FSC of 0.143.

Model building, refinement and validation, and structural analysis
The scFv76 structure was modeled with the Antibody Structure Prediction module using Schrödinger Maestro Bioluminate Suite 4.5.137, release 2021-4.[22] The modeling was performed with antigen-binding fragment (Fv) as antibody format. We used "EVQLLQ SAGGLVQPGGSLRLSCAASGFTVSANYMSWVRQAPGKGLEWV SVIYPGGSTFYADSVKGRFTISRDNSKNTLYLQMNSLRVEDTAV YYCARDLSVAGAFDIWGQGTLVTVSSGG" as the target sequence for the heavy chain (HC) and "IVLTQSPGTLSLSPGERATLSCRA SQSVSSSYLAWYQQKPGQAPRLLIYGASSRATGIPDRFSGSGSGT DFTLTISRLEPEDFAVYYCQQYGSSPYTFGQGTKLEIKRAAAGD

YK" for the light chain (LC). The tool identifies the best matching framework templates for the queried sequences and builds the CDR loops based on the cluster analysis performed on the default antibody loop database, sieved using the selected framework template. To select a suitable structural reference framework, we filtered the possible candidates according to the scFv76 HC and LC germlines, IGHV3-66 and IGKV3-20, respectively.[12] We analyzed 130 CoV-AbDab structures of antibodies (Abs) bound to RBDs[23] and found that 39 of 42 entries with IGHV3-53/IGHV3-66 HCs, usually coupled with IGKV1-9 (16 Abs) or IGKV3-20 (10 Abs) LCs, share a common binding mode to the RBD. The three outliers are characterized by longer CDR-H3 (17–25 residues compared with 8–15 residues), and they are bound to IGLV2-14/IGLV2-23 LCs. Based on these findings, and considering the good resolution (2.03 Å) and the average of HC and LC similarity scores (0.99 of 1.00), we selected PDB: 7N3I as the reference framework, whose HC and LC are a combination of IGHV3-53 and IGKV3-20. To model the scFv76 CDR loops as well as their interaction with the antigen, the CDRs were grafted into a homology modeled structure built based on the reference framework template that also included the N-terminal domain of the betacoronavirus-like trimeric spike glycoprotein S1 (PDB: 7N3I). The generated scFv76:RBD model was subsequently superimposed on the three RBDs of a SARS-CoV-2 HexaPro S cryo-EM structure, with two RBDs in the up and one in the down conformation (PDB: 7N0H). Finally, the three cryo-EM RBDs in complex with the modeled scFv76 were refined with Schrödinger Protein Preparation Wizard[24] to remove clashes and optimize side chains.

The generated model was split into two parts: the first comprised the whole spike protein without the RBDs; the second consisted of the RBD in the down conformation in complex with scFv76. Both models were independently refined with COOT[25] and PHENIX[26] using the full reconstruction and the local refined map at 3.5 Å and 4.0 Å resolution, respectively. Subsequently, the local refined RBD:scFv76 complex was rigid body fitted in the full spike:scFv76 reconstruction. All data collection, image processing, and final model statistics are summarized in Table S2. The images were prepared using ChimeraX[27] and Pymol (http://www.pymol.org/pymol).

Statistical analysis
Statistical analyses were performed using Prism software (v.6.0 or v.8.0, GraphPad). Data are presented as average ±SE or SD. Statistical significance was analyzed with unpaired two-tailed Student's t test, Mann-Whitney U test, or one-way analysis of variance (ANOVA). p values below 0.05 were considered statistically significant.

DATA AND CODE AVAILABILITY
The antibodies described in the paper can be provided upon material transfer agreement (MTA) subscription. The full spike:scFv76 and the RBD:scFv76 cryo-EM volumes and the structure coordinates have been deposited in the Electron Microscopy Data Bank and the Protein

Data Bank under accession codes EMDB: 14628 and EMDB: 14629 and PDB: 7ZCE and PDB: 7ZCF, respectively. Cryo-EM videos were deposited in the Electron Microscopy Public Image Archive under accession code EMPIAR: 10990.

SUPPLEMENTAL INFORMATION
Supplemental information can be found online at https://doi.org/10.1016/j.ymthe.2022.09.010.

DECLARATION OF INTERESTS
O.M., E.M.P., and R.D.S. are employees of Alfasigma SpA and are named as inventors in a patent application on the name of the same company.

REFERENCES
1. Araf, Y., Akter, F., Tang, Y.D., Fatemi, R., Parvez, M.S.A., Zheng, C., and Hossain, M.G. (2022). Omicron variant of SARS-CoV-2: genomics, transmissibility, and responses to current COVID-19 vaccines. J. Med. Virol. 94, 1825–1832. https://doi.org/10.1002/jmv.27588.

2. Markov, P.V., Katzourakis, A., and Stilianakis, N.I. (2022). Antigenic evolution will lead to new SARS-CoV-2 variants with unpredictable severity. Nat. Rev. Microbiol. 20, 251–252. https://doi.org/10.1038/s41579-022-00722-z.

3. Merad, M., Blish, C.A., Sallusto, F., and Iwasaki, A. (2022). The immunology and immunopathology of COVID-19. Science 375, 1122–1127. https://doi.org/10.1126/science.abm8108.

4. Iketani, S., Liu, L., Guo, Y., Liu, L., Chan, J.F.-W., Huang, Y., Wang, M., Luo, Y., Yu, J., Chu, H., et al. (2022). Antibody evasion properties of SARS-CoV-2 Omicron sublineages. Nature 604, 553–556. https://doi.org/10.1038/s41586-022-04594-4.

5. Liu, L., Iketani, S., Guo, Y., Chan, J.F.-W., Wang, M., Liu, L., Luo, Y., Chu, H., Huang, Y., Nair, M.S., et al. (2022). Striking antibody evasion manifested by the Omicron variant of SARS-CoV-2. Nature 602, 676–681. https://doi.org/10.1038/s41586-021-04388-0.

6. Planas, D., Saunders, N., Maes, P., Guivel-Benhassine, F., Planchais, C., Buchrieser, J., Bolland, W.-H., Porrot, F., Staropoli, I., Lemoine, F., et al. (2022). Considerable escape of SARS-CoV-2 Omicron to antibody neutralization. Nature 602, 671–675. https://doi.org/10.1038/s41586-021-04389-z.

7. Hoffmann, M., Krüger, N., Schulz, S., Cossmann, A., Rocha, C., Kempf, A., Nehlmeier, I., Graichen, L., Moldenhauer, A.-S., Winkler, M.S., et al. (2022). The Omicron variant is highly resistant against antibody-mediated neutralization: implications for control of the COVID-19 pandemic. Cell 185, 447–456.e11. https://doi.org/10.1016/j.cell.2021.12.032.

8. Cao, Y., Wang, J., Jian, F., Xiao, T., Song, W., Yisimayi, A., Huang, W., Li, Q., Wang, P., An, R., et al. (2022). Omicron escapes the majority of existing SARS-CoV-2 neutralizing antibodies. Nature 602, 657–663. https://doi.org/10.1038/s41586-021-04385-3.

9. VanBlargan, L.A., Errico, J.M., Halfmann, P.J., Zost, S.J., Crowe, J.E., Jr., Purcell, L.A., Kawaoka, Y., Corti, D., Fremont, D.H., and Diamond, M.S. (2022). An infectious SARS-CoV-2 B.1.1.529 Omicron virus escapes neutralization by therapeutic monoclonal antibodies. Nat. Med. 28, 490–495. https://doi.org/10.1038/s41591-021-01678-y.

10. Dejnirattisai, W., Huo, J., Zhou, D., Zahradník, J., Supasa, P., Liu, C., Duyvesteyn, H.M.E., Ginn, H.M., Mentzer, A.J., Tuekprakhon, A., et al. (2022). SARS-CoV-2 Omicron-B.1.1.529 leads to widespread escape from neutralizing antibody responses. Cell 185, 467–484.e15. https://doi.org/10.1016/j.cell.2021.12.046.

11. Shuai, H., Chan, J.F.-W., Hu, B., Chai, Y., Yuen, T.T.-T., Yin, F., Huang, X., Yoon, C., Hu, J.-C., Liu, H., et al. (2022). Attenuated replication and pathogenicity of SARS-CoV-2 B.1.1.529 Omicron. Nature 603, 693–699. https://doi.org/10.1038/s41586-022-04442-5.

12. Minenkova, O., Santapaola, D., Milazzo, F.M., Anastasi, A.M., Battistuzzi, G., Chiapparino, C., Rosi, A., Gritti, G., Borleri, G., Rambaldi, A., et al. (2022). Human inhalable antibody fragments neutralizing SARS-CoV-2 variants for COVID-19 therapy. Mol. Ther. 30, 1979–1993. https://doi.org/10.1016/j.ymthe.2022.02.013.

13. Yamasoba, D., Kimura, I., Nasser, H., Morioka, Y., Nao, N., Ito, J., Uriu, K., Tsuda, M., Zahradnik, J., Shirakawa, K., et al. (2022). Virological characteristics of the SARS-CoV-2 Omicron BA.2 spike. Cell 185, 2103–2115.e19. https://doi.org/10.1016/j.cell.2022.04.035.

14. Hsieh, C.-L., Goldsmith, J.A., Schaub, J.M., DiVenere, A.M., Kuo, H.C., Javanmardi, K., Le, K.C., Wrapp, D., Lee, A.G., Liu, Y., et al. (2020). Structure-based design of prefusion-stabilized SARS-CoV-2 spikes. Science 369, 1501–1505. https://doi.org/10.1126/science.abd0826.

15. Punjani, A., Rubinstein, J.L., Fleet, D.J., and Brubaker, M.A. (2017). cryoSPARC: algorithms for rapid unsupervised cryo-EM structure determination. Nat. Methods 14, 290–296. https://doi.org/10.1038/nmeth.4169.

16. Okuya, K., Hattori, T., Saito, T., Takadate, Y., Sasaki, M., Furuyama, W., Marzi, A., Ohiro, Y., Konno, S., Hattori, T., and Takada, A. (2022). Multiple routes of antibody-dependent enhancement of SARS-CoV-2 infection. Microbiol. Spectr. 10. e0155321-21. https://doi.org/10.1128/spectrum.01553-21.

17. Wang, Z., Deng, T., Zhang, Y., Niu, W., Nie, Q., Yang, S., Liu, P., Pei, P., Chen, L., Li, H., and Cao, B. (2022). ACE2 can act as the secondary receptor in the FcγR-dependent ADE of SARS-CoV-2 infection. iScience 25, 103720. https://doi.org/10.1016/j.isci.2021.103720.

18. Junqueira, C., Crespo, Â., Ranjbar, S., de Lacerda, L.B., Lewandrowski, M., Ingber, J., Parry, B., Ravid, S., Clark, S., Schrimpf, M.R., et al. (2022). FcγR-mediated SARS-CoV-2 infection of monocytes activates inflammation. Nature 606, 576–584. https://doi.org/10.1038/s41586-022-04702-4.

19. Tegally, H., Moir, M., Everatt, J., Giovanetti, M., Scheepers, C., Wilkinson, E., Subramoney, K., Moyo, S., Amoako, D.G., Baxter, C., et al. (2022). Continued emergence and evolution of Omicron in South Africa: new BA.4 and BA.5 lineages. Preprint at medRχiv. https://doi.org/10.1101/2022.05.01.22274406.

20. Riccio, A., Santopolo, S., Rossi, A., Piacentini, S., Rossignol, J.F., and Santoro, M.G. (2022). Impairment of SARS-CoV-2 spike glycoprotein maturation and fusion activity by nitazoxanide: an effect independent of spike variants emergence. Cell. Mol. Life Sci. 79, 227. https://doi.org/10.1007/s00018-022-04246-w.

21. Tegunov, D., and Cramer, P. (2019). Real-time cryo-electron microscopy data preprocessing with Warp. Nat. Methods 16, 1146–1152. https://doi.org/10.1038/s41592-019-0580-y.

22. Zhu, K., Day, T., Warshaviak, D., Murrett, C., Friesner, R., and Pearlman, D. (2014). Antibody structure determination using a combination of homology modeling, energy-based refinement, and loop prediction. Proteins 82, 1646–1655. https://doi.org/10.1002/prot.24551.

23. Raybould, M.I.J., Kovaltsuk, A., Marks, C., and Deane, C.M. (2021). CoV-AbDab: the coronavirus antibody database. Bioinformatics 37, 734–735. https://doi.org/10.1093/bioinformatics/btaa739.

24. Sastry, G.M., Adzhigirey, M., Day, T., Annabhimoju, R., and Sherman, W. (2013). Protein and ligand preparation: parameters, protocols, and influence on virtual

screening enrichments. J. Comput. Aided Mol. Des. *27*, 221–234. https://doi.org/10.1007/s10822-013-9644-8.

25. Emsley, P., Lohkamp, B., Scott, W.G., and Cowtan, K. (2010). Features and development of coot. Acta Crystallogr. D Biol. Crystallogr. *66*, 486–501. https://doi.org/10.1107/S0907444910007493.

26. Liebschner, D., Afonine, P.V., Baker, M.L., Bunkóczi, G., Chen, V.B., Croll, T.I., Hintze, B., Hung, L.W., Jain, S., McCoy, A.J., et al. (2019). Macromolecular structure determination using X-rays, neutrons and electrons: recent developments in Phenix. Acta Crystallogr. D Struct. Biol. *75*, 861–877. https://doi.org/10.1107/s2059798319011471.

27. Pettersen, E.F., Goddard, T.D., Huang, C.C., Meng, E.C., Couch, G.S., Croll, T.I., Morris, J.H., and Ferrin, T.E. (2021). UCSF ChimeraX: structure visualization for researchers, educators, and developers. Protein Sci. *30*, 70–82. https://doi.org/10.1002/pro.3943.

Supplemental Information

Spike mutation resilient scFv76 antibody

counteracts SARS-CoV-2 lung damage

upon aerosol delivery

Ferdinando M. Milazzo, Antonio Chaves-Sanjuan, Olga Minenkova, Daniela Santapaola, Anna M. Anastasi, Gianfranco Battistuzzi, Caterina Chiapparino, Antonio Rosi, Emilio Merlo Pich, Claudio Albertoni, Emanuele Marra, Laura Luberto, Cécile Viollet, Luigi G. Spagnoli, Anna Riccio, Antonio Rossi, M. Gabriella Santoro, Federico Ballabio, Cristina Paissoni, Carlo Camilloni, Martino Bolognesi, and Rita De Santis

Table S1. TaqMan gene assays (from Thermo Fisher Scientific) used for real time qPCR analyses.

Assay ID	Gene Symbol
Mm 00657574_s1	**ANGPT2**
Mm00441242_m1	**CCL2**
Mm01268754_m1	**CCL20**
Mm00486938_m1	**CDH5**
Mm03294838_g1	**COX2**
Mm01290062_m1	**CSF2**
Mm04207460_m1	**CXCL1**
Mm00445235_m1	**CXCL10**
Mm00438258_m1	**CXCR2**
Mm00516023_m1	**ICAM1**
Mm00515153_m1	**IFIT1**
Mm03030145_gH	**IFNA**
Mm00439552_s1	**IFNB**
Mm01168134_m1	**IFNG**
Mm00439620_m1	**IL1A**
Mm00434228_m1	**IL1B**
Mm00445259_m1	**IL4**
Mm00446190_m1	**IL6**
Mm01288386_m1	**IL10**
Mm00517640_m1	**IL21**
Mm01705338_s1	**ISG15**
Mm00487796_m1	**MX1**
Mm00840904_m1	**NLRP3**
Mm02528467_g1	**RLP32**
Mm00441278_m1	**SELE**
Mm00443258_m1	**TNF**
Mm01320970_m1	**VCAM1**

Table S2. Cryo-EM data collection, image processing and model refinement statistics.

Data collection and image processing

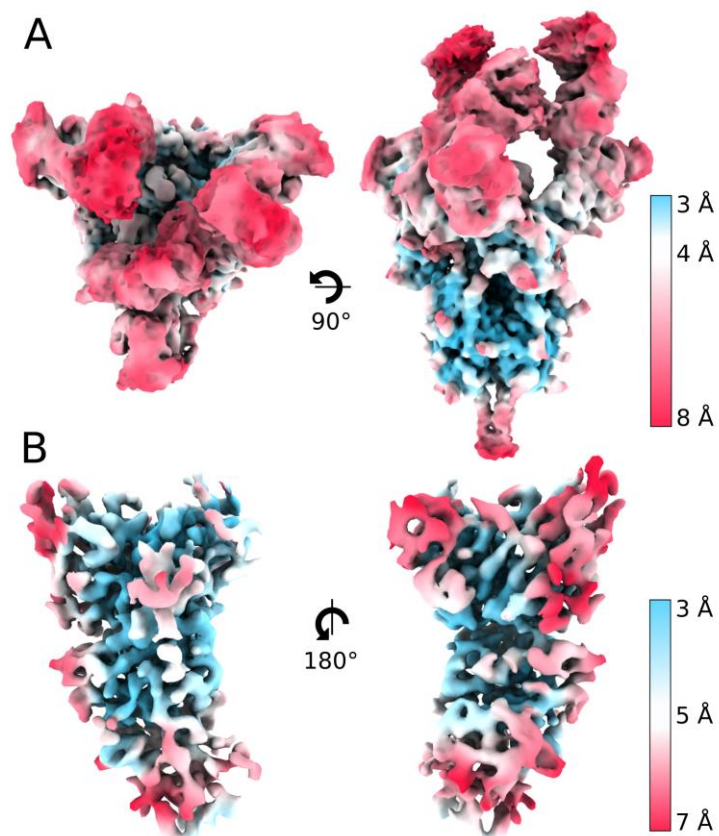| Structure	Spike:scFv76 full complex	RBD:scFv76 complex (Focused refinement)
Microscope	Thermo Fisher Scientific TALOS Arctica	
Voltage (kV)	200	
Camera	Falcon 3EC	
Magnification	× 120,000	
Total electron dose (e$^-$/Å^2)	40.0	
Defocus range (μm)	-0.8 and -2.2 μm	
Pixel size (Å)	0.889	
Micrographs (no.)	4,211	
Symmetry imposed	C1	C1
Initial particle images (no.)	490,614	87,623
Final particle images (no.)	87,623	87,623
Resolution (Å)	3.5	4.0
(FSC threshold)	(0.143)	(0.143)
Sharpening B-factor (Å^2)	-136.6	-157.9
EMDB code	EMD-14628	EMD-14629
Model refinement		
Protein residues	3706	426
N-acetyl-D-glucosamine molecules	51	1
r.m.s. deviations		
Bond lengths (Å)	0.004	0.002
Bond angles (°)	0.663	0.643
Ramachandran plot		
Favored (%)	91.42	85.24
Allowed (%)	8.58	14.76
Disallowed (%)	0.00	0.00
Validation		
Molprobity score	1.96	2.18
Clashscore	8.35	10.15
Poor rotamers (%)	0.03	0.56
Map-model correlation	0.84	0.72
PDB code	7ZCE	7ZCF

Figure S1. Local resolution cryo-EM map. A) spike:scFv76 full complex top and sides views. B) Locally refined RBD:scFv76 in the closed conformation, front and back views. Maps are colored according to the estimated local resolution.
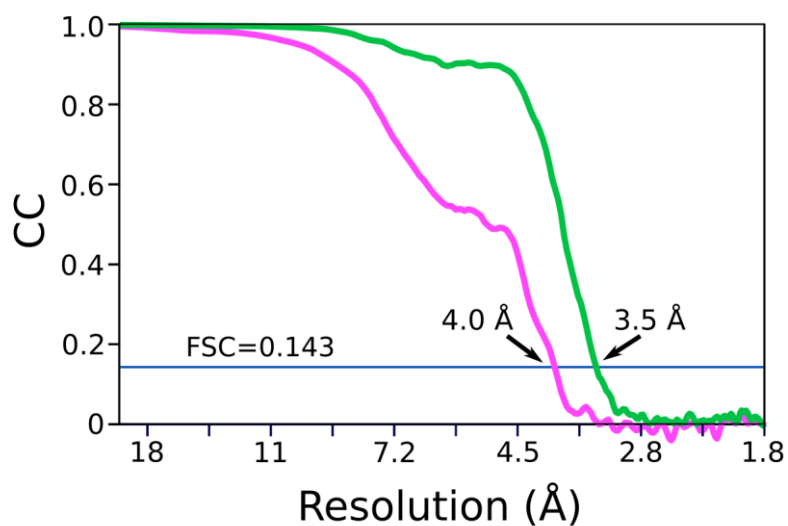

Figure S2. Cryo-EM FSC curves of spike:scFv76. The FSC curves for the spike:scFv76 full complex and the locally refined RBD:scFv76 in the closed conformation are shown in green and pink, respectively. The 0.143 threshold and the resolution cut-off for each curve are indicated.
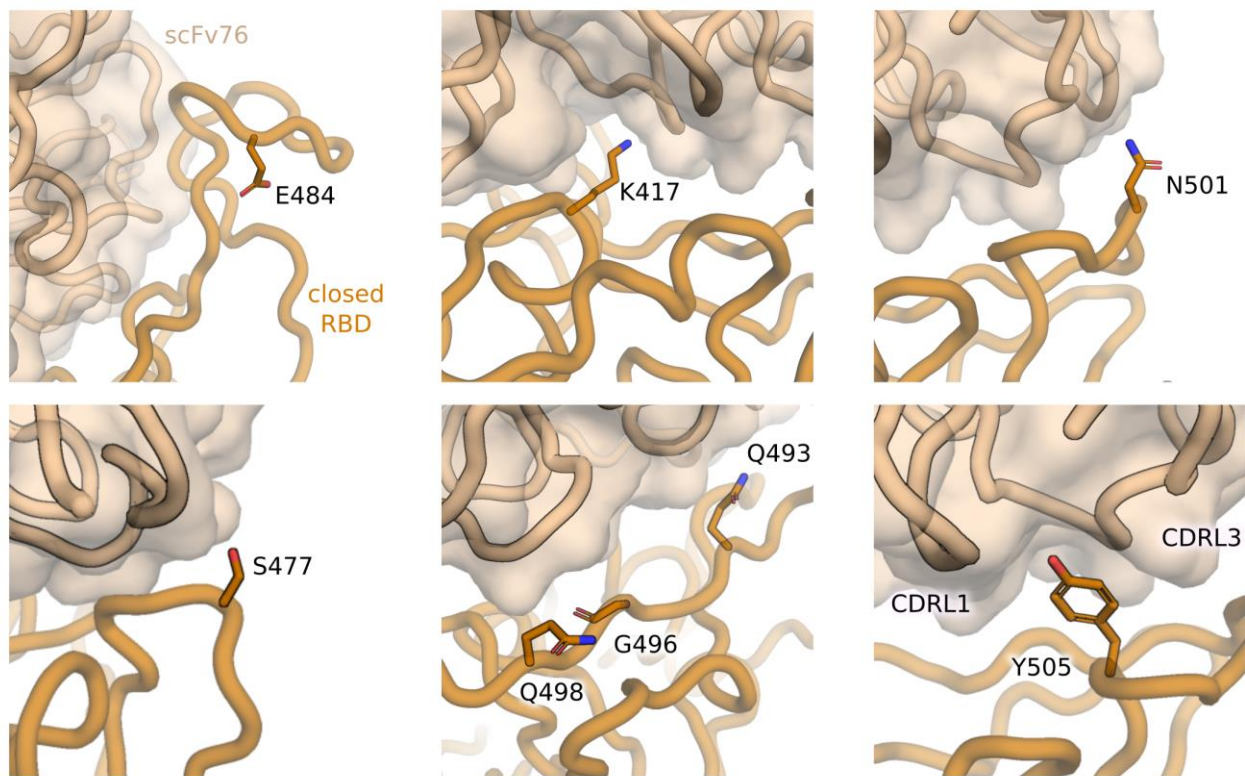
Figure S3. SARS-CoV-2 variants mutations at the RBD:scFv76 interface. Cartoon representation of scFv76 (transparent surface and worm) bound to the closed RBD (worm model); highlighted are key mutated residues (shown as stick models) in SARS-CoV-2 Omicron BA.1 and BA.2 variants.